



## Article

# A Comparison of Volumetric Reconstruction Methods of Archaeological Deposits Using Point-Cloud Data from Ahuahu, Aotearoa New Zealand

Joshua Emmitt <sup>1,\*</sup> , Patricia Pillay <sup>1,2</sup>, Matthew Barrett <sup>1</sup> , Stacey Middleton <sup>1</sup>, Timothy Mackrell <sup>1</sup>, Bruce Floyd <sup>1</sup> and Thegn N. Ladefoged <sup>1,2</sup>

<sup>1</sup> School of Social Sciences, University of Auckland, Auckland 1010, New Zealand; ppil534@aucklanduni.ac.nz (P.P.); matthew.barrett@auckland.ac.nz (M.B.); stacey.middleton@auckland.ac.nz (S.M.); t.mackrell@auckland.ac.nz (T.M.); b.floyd@auckland.ac.nz (B.F.); t.ladefoged@auckland.ac.nz (T.N.L.)  
<sup>2</sup> Te Pūnaha Matatini, Private Bag 92019, Auckland 1101, New Zealand  
\* Correspondence: josh.emmitt@auckland.ac.nz

**Abstract:** Collection of 3D data in archaeology is a long-standing practice. Traditionally, the focus of these data has been visualization as opposed to analysis. Three-dimensional data are often recorded during archaeological excavations, with the provenience of deposits, features, and artefacts documented by a variety of methods. Simple analysis of 3D data includes calculating the volumes of bound entities, such as deposits and features, and determining the spatial relationships of artifacts within these. The construction of these volumes presents challenges that originate in computer-aided design (CAD) but have implications for how data are used in archaeological analysis. We evaluate 3D construction processes using data from Waitetoke, Ahuahu Great Mercury Island, Aotearoa, New Zealand. Point clouds created with data collected by total station, photogrammetry, and terrestrial LiDAR using simultaneous localization and mapping (SLAM) are compared, as well as different methods for generating surface area and volumes with triangulated meshes and convex hulls. The differences between methods are evaluated and assessed in relation to analyzing artifact densities within deposits. While each method of 3D data acquisition and modeling has advantages in terms of accuracy and precision, other factors such as data collection and processing times must be considered when deciding on the most suitable.

**Keywords:** 3D data; simultaneous localization and mapping; photogrammetry; total station recording; volumetric analysis; artefact density; New Zealand Archaeology; Ahuahu Great Mercury Island



**Citation:** Emmitt, J.; Pillay, P.; Barrett, M.; Middleton, S.; Mackrell, T.; Floyd, B.; Ladefoged, T.N. A Comparison of Volumetric Reconstruction Methods of Archaeological Deposits Using Point-Cloud Data from Ahuahu, Aotearoa New Zealand. *Remote Sens.* **2021**, *13*, 4015. <https://doi.org/10.3390/rs13194015>

Academic Editors: Jesse Casana and Elise Jakoby Laugier

Received: 15 September 2021

Accepted: 1 October 2021

Published: 7 October 2021

**Publisher's Note:** MDPI stays neutral with regard to jurisdictional claims in published maps and institutional affiliations.



**Copyright:** © 2021 by the authors. Licensee MDPI, Basel, Switzerland. This article is an open access article distributed under the terms and conditions of the Creative Commons Attribution (CC BY) license (<https://creativecommons.org/licenses/by/4.0/>).

## 1. Introduction

Three-dimensional recording in archaeology is an increasingly applied and accessible methodology. The reduction in costs of specialized equipment and computing power, in addition to simplified workflows, has meant that such recording methods can be applied in a wide range of contexts (e.g., [1–5]). Volumetric calculations are one of the goals of 3D recording, the ability to digitally define the volume that is being investigated, whether it be a sedimentary deposit or an architectural wall [6,7]. Aside from visualization, volumes can be utilized for calculating densities of artefacts in deposits, which aid in interpretations of formational histories and use of place [6]. Different methods can be used to record and create volumes to various levels of detail. These differences require quantification to determine what influence, if any, they have on the creation of volumes. In this paper, we compare surface areas and volumes created with data collected by three different methods commonly employed in archaeological inquiry: total station (TS), light detection and ranging (LiDAR) using simultaneous localization and mapping (SLAM), and photogrammetry (PG). We also compare two modeling methods that are readily available in a range of software, triangulated meshes and convex hulls, to test what effect these have on the resulting

volumes and artifact densities. The process for constructing the volumes is discussed, along with comment on the most time and cost effective of the methodologies.

## 2. 3D Data Recording

There are a variety of methods to record archaeological phenomena during excavation and survey. Analogue methods record 3D information in relation to a grid placed over an area. A tape measure was often used to determine x and y coordinates with elevation measured in relation to a common datum, whether that is the ground level or survey marker. Dumpy levels, transits, plane-table alidades, and other instruments can improve precision and accuracy of these measurements. Beginning in the 1980s, the use of TS with built-in or external data loggers significantly reduced the amount of time it took to take measurements [8,9]. This resulted in an increase in the number of readings and, in turn, new excavation techniques [9,10]. Using TS, thousands of measurements can be taken in a relatively short time to create point-cloud data.

TS are now a common archaeological recording tool and are used in a range of contexts (e.g., [11,12]). This has been due to an increase in the interest and utilization of 3D data for the analysis of artefact distributions (e.g., [13]) and topological analyses. While the recording of artefact positions has largely stayed within the purview of TS recording, recording 3D data related to landscapes and features has increasingly utilized LiDAR and structure from motion (SfM).

There are many archaeological applications of LiDAR which fall under two broad categories, airborne LiDAR survey (ALS) and terrestrial LiDAR survey (TLS). ALS has historically been done by aircraft at the landscape scale (see [14] for a recent review) with more recent use of drones [14–17]. TLS involves the use of ground-based LiDAR systems; however, given the increasing use of drones for LiDAR capture, this division is becoming obscured as aerial drones capture data that terrestrial systems could have [14]. Archaeological applications of TLS include small-scale landscape features such as mounds, but also smaller entities such as archaeological excavations [18–20]. ALS and TLS create point clouds by aligning common points that are relative to what they are recording. A method for interpolating LiDAR data is simultaneous localization and mapping (SLAM), which creates a point cloud of an area relative to the position of the recording device within it and the features it records. In archaeology, SLAM is most commonly applied to built environments with architectural features [21], but has also been used in underwater archaeology [22].

Modelling using SfM, otherwise commonly referred to as photogrammetry (PG), is increasingly common in archaeological inquiry [23]. This technique utilizes multiple photographs around a common object or feature to create a 3D point cloud, which can consist of thousands or hundreds of millions of points [24]. Both objects [1,4] and features [25,26] are frequently digitized in this way, and photogrammetry is applied to excavations as well as wider built and natural landscape contexts [27–30]. These data are most commonly employed as aids for interpretation or for visualization as 2.5D objects, which is an otherwise 2D dataset that is represented as a 3D model, although some work has been done on making 3D volumes from the data (e.g., [31]). Despite this, analytical applications of created volumes are generally lacking, a point we return to below.

There are known, yet generally unquantified, advantages and disadvantages to these three methods (TS, PG, and LIDAR (specifically SLAM)). PG provides an accurate alternative to other forms of recording such as total stations for surfaces [32]. In other examples where data are collected on objects, PG was found to be more accurate than laser scanning [3,33]. In a comparison between ALS, PG, and radar for measuring water surface elevation, radar was found to be the most accurate but LIDAR vs. PG were similar [34].

PG is also an efficient technique for acquiring data, as it generally takes up less physical space than other methods. The space available for recording may be a factor in this, as small spaces may be better captured with photogrammetry and can later be merged with wider larger scans obtained through TLS [35]. PG models are also used to

colorize data captured from ALS or TLS [36–38] and, in some cases, enhance the resolution of particular features [39]. Modern LiDAR systems such as SLAM, however, increasingly employ color capture without the use of PG [40]. Despite the advances in LiDAR, PG is still generally less expensive than other approaches and, therefore, more widely accessible. This is particularly the case when it is applied terrestrially [35].

All three methods (TS, PG, and LIDAR (specifically SLAM)) can be used to construct point clouds, which may in turn be triangulated into meshes. The point clouds generated by TS [11] are generally coarse in comparison to PG or SLAM. Collecting smaller quantities of data, yet often enough for analysis, can be quicker with TS than the other methods. TS also has the advantage that it is generally quicker and more easily integrated into existing workflows for small areas. Obtaining large quantities of data via TS, however, can be much more time consuming in relation to PG and SLAM.

Where physical space is available and excavation areas allow, artefact provenance data can be extracted from 3D models [32]. Time and excavation methods again have an influence here as the ability to pedestal objects may be limited by their density or the recording practice of only creating models at the interface of deposits or features. Time is also a factor, which is essential to consider when applying differing methodologies, as some are more labor intensive in-field, while others are labor intensive off-site. In the case of PG, Scott and colleagues [31] highlight that in some cases, the amount of time taken to record and process a 3D model of small objects can be larger than the time taken to excavate the object.

### 3. Uses of 3D Data

Data collected with TS, PG, or LiDAR and the resultant 3D models are either displayed on their own or in conjunction with other forms of geospatial data in a geographical information system (GIS) interface [2,30,41,42]. With respect to the built environment, one of the frequent uses of 3D data is the reconstruction of buildings, which are used for visualization and analytical purposes [26,42,43]. The data represented, however, are rarely actually “3D” and, instead, consist of what is referred to as “2.5D”. The key difference is that a 3D model has a bounded volume, it closes back on itself, whereas a 2.5D model does not. A common application of 2.5D models are landscapes, which in order to “close”, would require a model of the entire planet. Examples of 3D models would include an artefact where the whole object is represented or, in the case of this paper, a deposit identified during excavation.

Roosevelt and colleagues [44] created volumes from PG 3D data to record deposits, and their stratigraphic relationships, however, do not suggest any analytical use for such volumes. Gavryushkina [7] used ESRI ArcGIS to construct 3D volumes from deposit outlines that were extruded to create closed entities. They compared multiple methods of volume creation including triangulated irregular networks (TIN), minimum bounding volume, and digitized section drawings. It was found that the volumes calculated from each were different, the volumes from TINs were successful when available, but the construction method depended on the x and y alignment of the TINs, which as noted elsewhere, is not always the case [6]. The minimum bounding volumes tended to over-represent the volume of the deposits, while the stratigraphic drawings were not carried out in enough frequency to capture the deposits in enough detail.

Interpreting stratigraphic relationships is one of the more frequently cited reasons for creating 3D excavation data [45] and certainly has utility [6,46]. In addition, 3D data can be used to create deposit volumes for understanding differential patterning in artifact distributions. However, the construction of a deposit volume is contingent upon a number of factors including how data were collected and processed. The influence that these factors can have on the calculation of volumes and the interpretations from them requires further analysis. Here, we compare the use of triangulated meshes and convex hulls to model deposit surface areas and volumes created from TS, PG, and SLAM data.

#### 4. Case Study: Waitetoke, Ahuahu Great Mercury Island

Ahuahu Great Mercury Island lies c. 5.5 km off the east coast of the Coromandel Peninsula of the North Island, Aotearoa New Zealand (Figure 1). It is composed of elevated land to the north and south of volcanic origin with a central tombolo of sand. The island has considerable evidence for Māori occupation. Initial research on the island focused on pā (fortifications) around the coast in addition to the general identification of archaeological sites and features [47–51]. Since 2012, the Ahuahu Great Mercury Island Project has carried out surveys and excavations across the northern half of the island with most attention focused around the tombolo area [18,52–61].

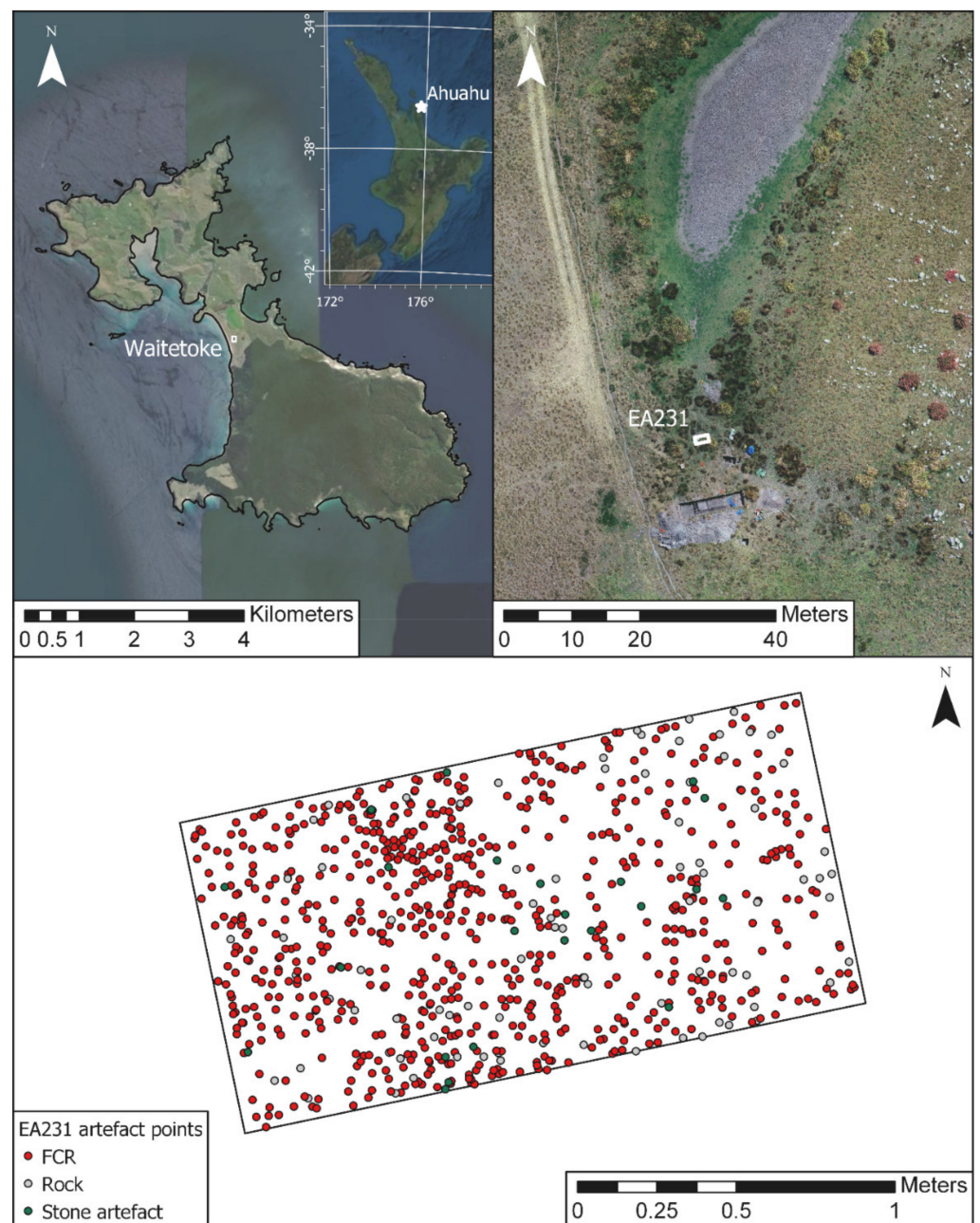


**Figure 1.** Location of Ahuahu Great Mercury Island and Waitetoke, with the distribution of all artefacts and features recorded from EA231. FCR = fire-cracked rock.

Waitetoke (NZ SRS# T10/356) is a particular location of interest for understanding horticultural development on the island. It is in a swale between dunes and a hill slope at

the southern end of the tombolo (Figure 1). Excavations in 2012 at Waitetoke investigated a series of stone rows and rock-faced terraces on the slope to the south of a current mire. This area was used for kūmara (sweet potato; *Ipomoea batatas*) production utilizing a number of different techniques [52]. Shovel test pitting of the mire in 2012 and coring and excavation at EA200 in 2015 identified early evidence for taro (*Colocasia esculenta*) production, and dating of sedge seeds associated with fire-cracked rock and charcoal provided a date of 1434–1488 CE (Wk47862,  $469 \pm 19$ , calibrated with SHCal20, 95.4% 516–462 BP) [55,57].

Excavations resumed at Waitetoke in 2019 and again in 2020 to further examine the extent of horticultural features to the southwest of the mire. Several excavations were done that identified a system of channels, small check dams or weirs, and anthropogenic garden sediments, all used in taro production. In April 2021, further excavations were carried out with the dual aim of determining the extent of the channel system as well as testing new recording practices. Here, we report on the methods of data acquisition utilized and test their applicability to the recording of one of the trenches, EA231 a  $1 \times 2\text{m}$  unit (Figure 1).

Our recording practice at EA231 followed a spatial-hierarchical system that defines two base observations, objects and features [61]. An object is defined as something that can be picked up and moved, and a feature is something that cannot, such as a channel feature. Objects and features are attributed to a deposit, defined as a homogenous sedimentary matrix, which in turn exists within an excavation area (EA). Each entity is given a unique identifier (UNID).

EA231 was excavated to investigate the extent of a secondary channel (Feature 30754) off the main channel system. During the excavation of EA231, eight primary sedimentary deposits were identified (Figure 2), with an underlying culturally sterile deposit not modelled or shown in our analysis, aside from forming the base of layers 7 and 8. Additional deposits in EA231 were recorded during the excavation and when profiles were drawn, but these are not included in our analysis in this paper. Our field recording schema assigned a unique identifier (UNID) to the deposits, and a relative numbering system has been assigned for this analysis (Table 1). Varying numbers of fire-cracked rock (FCR) and stone artefacts and rocks were recorded during excavation (Table 1).

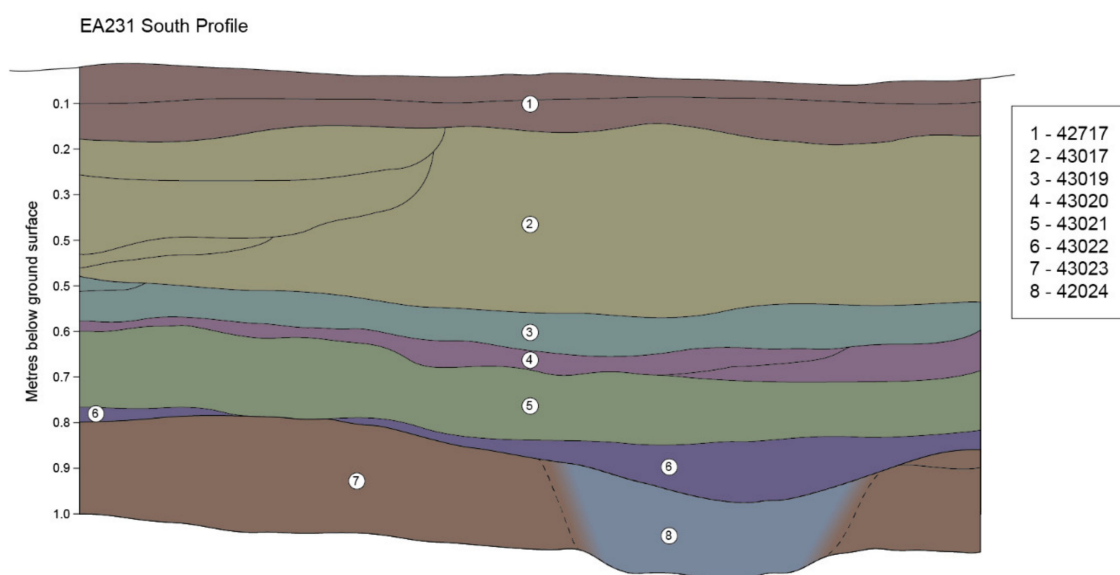


**Figure 2.** The stratigraphic sequence of EA231 with layer numbers. Un-numbered layers were either combined for this analysis or identified during the section drawing but not during excavation.

**Table 1.** Artefacts excavated from EA231 by deposit, with deposit numbers and their relative associations. FCR = fire-cracked rock; SA = stone artefact.

Layer	Deposit	FCR	Rock	SA	Total
1	42717	10	1	2	13
2	43017	76	13	5	94
3	43019	33	3	1	37
4	43020	9	1	0	10
5	43021	6	0	2	8
6	43022	0	0	1	1
7	43023	83	21	7	111
8	42024	3	1	1	5

## 5. Data Acquisition and Processing

During the excavation of EA231, three methods of data acquisition (TS, PG, and LIDAR (SLAM)) were used either as a matter of standard recording or to test their potential to improve workflow. While the project has used terrestrial LiDAR to record landscapes and larger architectural features (e.g., [18]), our usual excavation recording system [61] involves measurements with a total station. We record the surface of deposits and features, as well as the cuts of features, with their extent recorded as a polygon and the internal variation within them recorded as points. Every object identified during excavation measuring 2–20 cm is recorded as a point, and larger objects are recorded as a polygon to capture their extent. Smaller objects are attributed to a single sample bag, which are related to the deposit or feature. Material recovered during sieving is likewise inventoried.

The excavation of EA231 began with de-turfing of the trench, with an extra ca. 25 cm on each side de-turfed to create a stable edge for the alignment of points (Figure 3). This was necessary, as earlier tests of the equipment indicated that overhanging grass adversely affects model alignment. Below, we outline each of the three methods (TS; PG; SLAM) used to acquire and process the 3D data. Each method was repeated for the eight primary deposits in the trench, and surface areas and volumes were calculated.



**Figure 3.** EA231 at the point of recording layer 6. An extra ca. 25 cm has been de-turfed to create a stable edge to the trench. PG targets are around the trench and on the Y fence posts. The GeoSLAM Zeb Horizon is located on one of the base points, with the others marked by pink flagging tape.

### 5.1. Total Station

The traditional method of recording excavation data during the Ahuahu Archaeological Project is with a total station [61]. For the excavation of EA231, we used a Trimble S7 Robotic Total Station (Sunnyvale, CA, USA) to record the locations of artefacts, outlines of samples and deposits, and surfaces (of deposits and features). Surfaces were recorded over a triangular grid pattern with points no more than 25 cm apart. When areas with more variable topography were encountered, such as for a feature, this resolution was increased. Raw total station points were processed through the software Trimble Business Center v5.50 (Trimble, Sunnyvale, CA, USA) and exported as ESRI point shapefiles constituting point clouds.

### 5.2. Photogrammetry

A Canon EOS 800D (Ota City, Tokyo, Japan) camera with a Canon Zoom Lens EF-S 18–55 mm was used to take photographs for PG. The focal length was set at 18 mm for most passes across a trench, but may have been increased for some rotations due to logistical constraints of photographing the interior of the trench. Approximately 100–250 photographs were taken per model. The general approach was to take photos every 20 degrees around the 1x2m trench, equivalent to approximately a small step. A series of top-down photographs were also taken across the trench, which would result in a general model, and to which photographs of specific features that may require more detail could be applied (Figure 4). Targets were printed from Agisoft Metashape 1.7.2. [62], laminated, and placed around the trench in the middle of each edge. In addition, two metal “Y” fence posts were put into the ground at two opposing ends of the trench with several targets attached (Figure 3). The use of 12 targets was necessary for redundancy and georectification. The center of the targets on the ground were recorded with a total station, whereas the targets on the poles were only used to aid in the alignment of the photos and between models. All targets were left in place for the course of the excavation.



**Figure 4.** Example of the location of targets around a trench and the distribution of photographs taken to construct a model. The model depicted is that used for layer 6.

Agisoft Metashape 1.7.2. [62] was used to create the photogrammetric models. Photos were aligned at the highest accuracy to create a sparse set of tie points. The tie points were processed with variables, reprojection error of 0.5 px, reconstruction uncertainty of 15 px,

image count of 2, and projection accuracy of 2.5 px. These variables were applied to all deposits except for the turf (Layer 1), where a reconstruction uncertainty of 50 was required to have enough points to construct a dense cloud. The dense cloud for all deposits was constructed at ultra-high quality as was the resulting 3D model, with the latter limited to a face count of 500,000.

### 5.3. SLAM

We used a GeoSLAM Zeb Horizon (Nottingham, United Kingdom) to capture SLAM TLS data (Figure 3). Initial tests incorporated four base points at the top corners of the trench; however, this was found to be insufficient to record the interior of the trench. A fifth base point was added to the interior of the trench, which allowed for capture of the depth and the walls. Each of the base points outside the trench was recorded with TS for georectification. These data were processed in the software GeoSLAM Hub 3.5 and GeoSLAM Draw 3.2 R2 (GeoSLAM Inc., Sterling, VA, USA), which allowed for the georeferencing of the base points and alignment of the scans.

The SLAM data contained a high number of points, which made it difficult to create surfaces and define volumes, as the irregular shape of the trench caused uncertainty in the alignment. To mitigate this, CloudCompare 2.11.2 and the proprietary software Geomagic Wrap 2021 were used to clean the point cloud. Outlying points were manually removed to the general shape of the trench, before applying the “Reduce Noise” tool, which gradually removes outlying points. This was done until a surface was achieved in the point cloud. The resulting point cloud was then meshed, normals recalculated, and the volume calculated.

## 6. Surface and Volume Construction

The creation and depiction of volumes falls under two broad categories, the idealized and the actual.

### 6.1. Idealized Volumes

Idealized volumes use surface data of the top and bottom surfaces with a straight relationship established between them. Such interpretations are made when using archival data [46,63] but also when data are visualized generally (e.g., [7]). These visualizations also occur when volumes are constructed from two 2.5D rasters or layer surfaces [6,11,64]. Such data are represented here by the TS surface reconstructions.

To construct the TS surfaces, point clouds were imported into Blender 2.9 (Blender Foundation, Amsterdam, The Netherlands) with the Blender GIS add-on. The surfaces were created through a Delunany triangulation, which created a 2.5D entity. Two surfaces were attached to each other to create a straight wall and a bounded volume of the deposit represented.

### 6.2. Actual Volumes

In contrast to idealized volumes, actual volumes are calculated when the walls of a volume are considered, creating a 3D volume of the deposit as it were an entity. The walls may either be arbitrary, such as the edge of a trench, or informed, such as the end of a deposit or the edge of a feature [44]. While excavators aim to create straight baulks in their excavations, trenches can either be undercut, “bathtubbed”, or have other deviations due to objects or variations from excavation. These factors, while perhaps minimal, all affect any volumes that may be calculated; however, the degree to which they do is tested and discussed below.

The SLAM data were processed in Geomagic Wrap, and the PG models in Agisoft Metashape 1.7.2. [62]. In each case, the top and bottom of a deposit were joined together, and then, any trench walls present above the top deposit were manually edited out. This resulted in two separate components, which represent but do not create a bounded volume. The SLAM data were meshed in Geomagic wrap to create a bounded volume with normals, and then, volume was calculated from these.

For PG, the data were exported as a ply to the computer-aided design (CAD) software Blender 2.9 (Blender Foundation, Amsterdam, The Netherlands) where the “remesh” modified with an Octree level of 8 was used to reconstruct a closed volume. Due to the excavation process, there was in some cases a gap between the extent of the top deposit and the corresponding walls from the bottom deposit, which an Octree reconstruction could not join. In these cases, the edge of the top deposit was extruded across to be closer to the wall so that a complete volume would be created. Once a volume was achieved, normals were recalculated for the mesh and volume calculated using the built-in 3D Print Toolbox.

Additional convex hull volume entities were created from the three (TS, PG, SLAM) point cloud datasets. Convex hulls model volumes by creating a mesh over a point cloud that represents the smallest convex surface area possible and are in many cases quicker to create than a triangulated mesh as the data require less cleaning. Meshlab 2020.06 [65] was used to create the convex hulls of each deposit and calculate surface areas and volumes for them. A convex hull was also created for the artefact points, recorded by TS, attributed to each deposit, to investigate if this would be an acceptable substitute for surface recording of deposits.

The scripts and data used in the below statistical analyses are available in File S1.

## 7. Results

Examination of the 3D representations of the deposits in the trench shows considerable variability in the models created with TS, PG, and SLAM data (Figure 5). The comparative analysis suggests that the SLAM technology is not well suited towards irregular, relatively small shapes, particularly within a natural environment such as the sand dune swale at Waitetoke without regular surfaces such as those found on buildings and some rock formations. The point clouds generated from the device and associated software had multiple vertical and horizontal “layers” of points within which were several indistinguishable surfaces, as the algorithm could not identify “features” to align the data to. Cleaning was attempted in CloudCompare but noise-reducing filters were again unable to create a surface for each scan. Eventually, the software Geomagic was used to average points to make a single surface for the triangulated mesh, which was used in further processing. As shown in Figure 5, this mesh is not as smooth as the PG model and has much more surface variation than the PG model, but this variation does not represent the actual surfaces of the deposits. The TS data represented the maximum extents of the excavation of a layer on the x and y axes. Compared to the PG and SLAM models, however, the surface data were of a lower resolution as a result of the way it was collected and, therefore, shows less detail.

The convex hull models created from the point clouds of the three different methods look similar to each other, with the total station model looking the most complete as the points used represent the maximum extent of the excavation. The convex hull created from the artefact point cloud is the least accurate representation of the deposit. Those models of deposits are based on the artifacts contained within the deposit, with artifacts very rarely located at the maximum extent of deposits. In general, compared to the triangulated meshes of the point clouds of the three acquisition methods (TS, PG, SLAM), the convex hulls lose the internal variation of surfaces, as many of these form concave shapes.

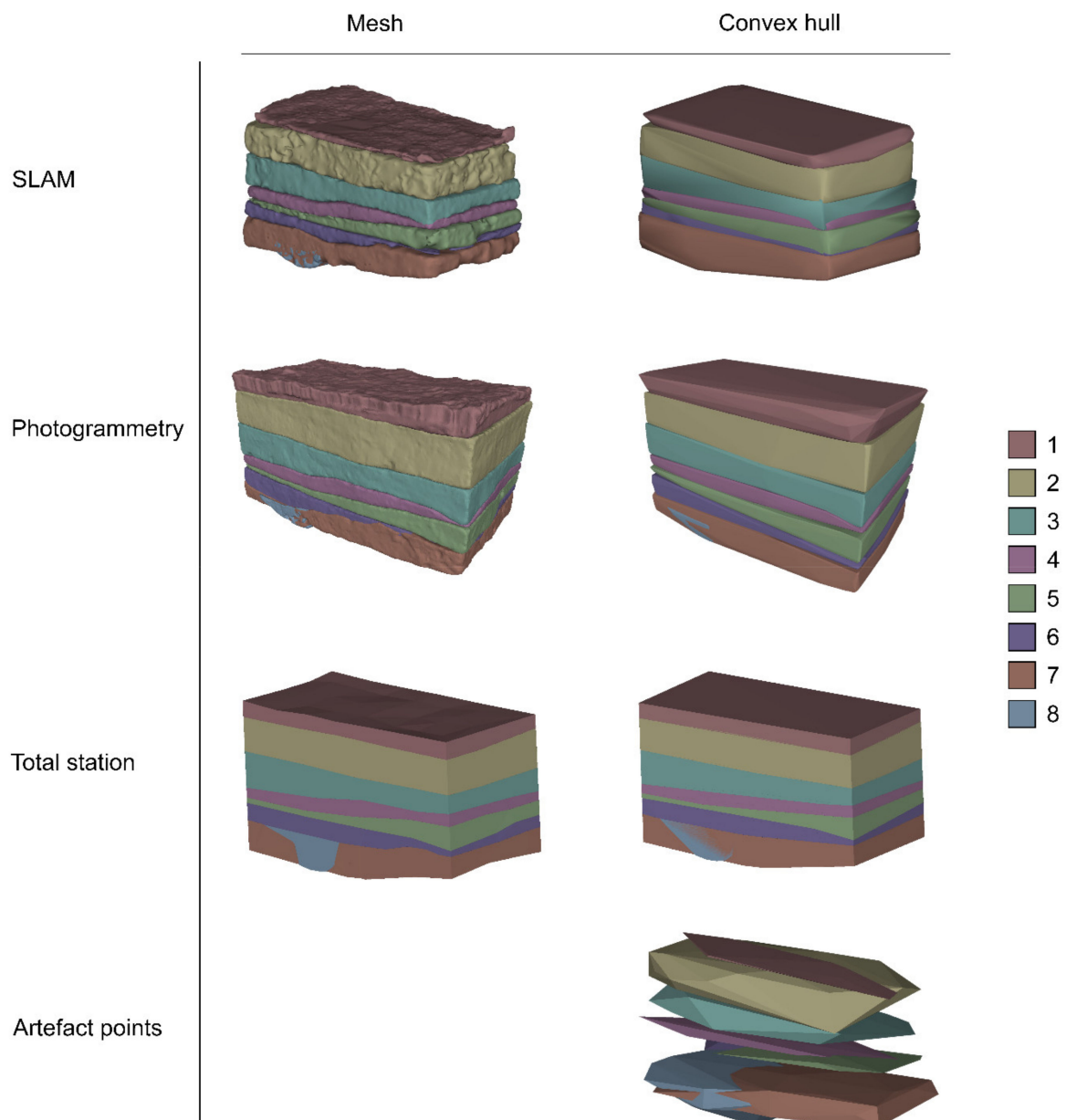


**Figure 5.** 3D views of EA231 from the different methods used.

### 7.1. Surface Comparison

To evaluate the difference between the triangulated meshed surfaces of the three methods the distances between the meshes of the deposits created with the three methods were measured in CloudCompare. In Figures 6 and 7, the PG model of the deposits were used as the base in the comparisons for the SLAM and TS models. There are some discrepancies between the SLAM and PG models, particularly around the edges, corners, and sides of the models (Figure 6). This is also the case for thinner areas where the averaging used to clean the SLAM point cloud resulted in overlap between the top and bottom surfaces. Layer 5 in Figure 6 depicts this on the inverse view in red; however, there are also holes in the PG model demonstrating that this area was so thin that it too had an issue creating separate deposits, albeit to a lesser degree.

Unsurprisingly, there are also discrepancies between the TS and PG models, particularly considering smaller details. The walls on the TS models were flat, and therefore,

differences are shown to the PG model that was not. Layer 1 represented in Figure 7 also shows where smaller differences are apparent such as the grass present on the surface (shown as red), which was captured by PG but because of the resolution was not captured by TS. Comparison of the TS and SLAM models shows similar results to that of the TS and PG (Figure 8). The walls are still a source of difference because of the basic lack of data for them in the TS models. Layer 2 in Figure 8 shows a high level of discrepancy between the TS to the SLAM model, and the lack of agreement between the two demonstrates the inability of the SLAM data to identify a surface in this case.

Table 2 reports estimates of surface area in m<sup>2</sup> by deposit for each method across modelling techniques. Paired *t*-tests or Wilcoxon signed-ranks tests were used to statistically assess pair-wise differences in estimated surface areas within deposits for three methods (SLAM, PG, or TS) across the two modelling techniques, triangulated mesh and convex hull. The test used was based on the results of a Shapiro–Wilk test for normality (Table 3). The results in the first section of Table 3 indicate that there are no significant differences in the surface areas of deposits between the meshed SLAM, PG, and TS models when each mesh model is compared with another mesh model. Counter to this are the visual differences between the triangulated meshes for PG and SLAM data discussed above (Figure 6), which suggests that the differences are largely visual. The results in the second section of Table 3 indicate that within each method, surface areas estimated using convex hulls are consistently greater than those estimated using triangulated mesh. This suggests that those convex hull models are over-representing the true extent of the deposits. Results in the third section of the table indicate that there are significant differences in the surface areas of deposits between the convex hull SLAM, PG, and TS models when each convex hull model is compared with another convex hull model. It seems that the over estimation of surface areas of the convex hull models of deposits of the individual methods is enough to establish differences between the three methods in a comparison of the convex hull models by method.

**Table 2.** Surface areas of each layer by method and modelling technique in m<sup>2</sup>.

Deposit	Triangulated Mesh			Convex Hull			Artefacts
	SLAM	PG	TS	SLAM	PG	TS	
1	4.533	4.781	4.753	5.198	4.997	4.800	1.41
2	5.801	5.735	5.664	6.186	5.895	5.692	3.84
3	5.328	5.491	5.273	5.772	5.717	5.355	3.14
4	4.653	4.762	4.578	5.072	4.950	4.630	1.77
5	4.630	4.693	4.495	5.185	4.963	4.628	1.39
6	4.698	5.045	4.771	5.202	5.279	4.812	0.31
7	5.394	5.491	4.593	6.100	5.723	5.380	3.86
8	1.901	1.795	1.985	1.970	1.873	2.025	2.41

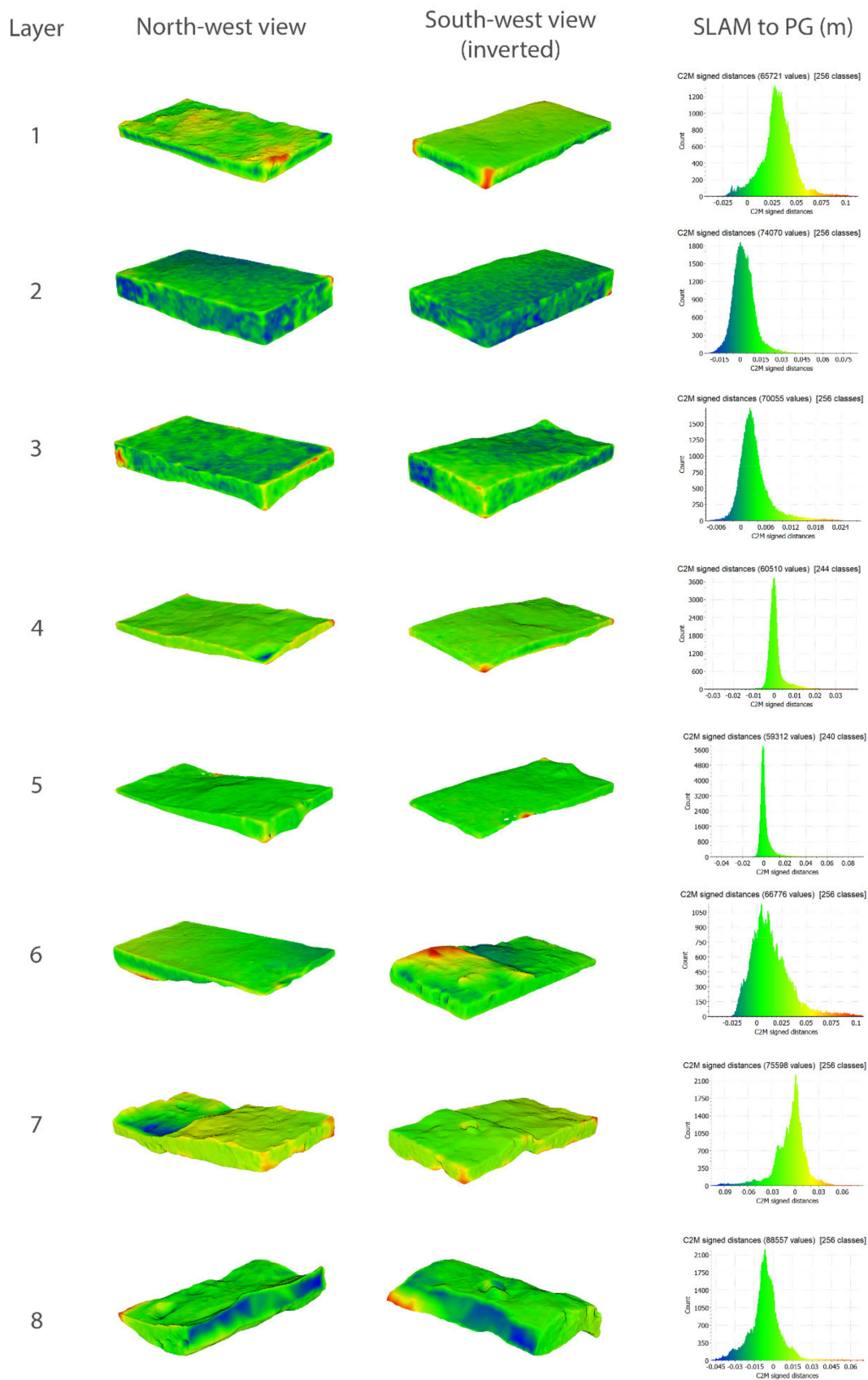


Figure 6. Comparison of the SLAM mesh onto the PG mesh by layer.

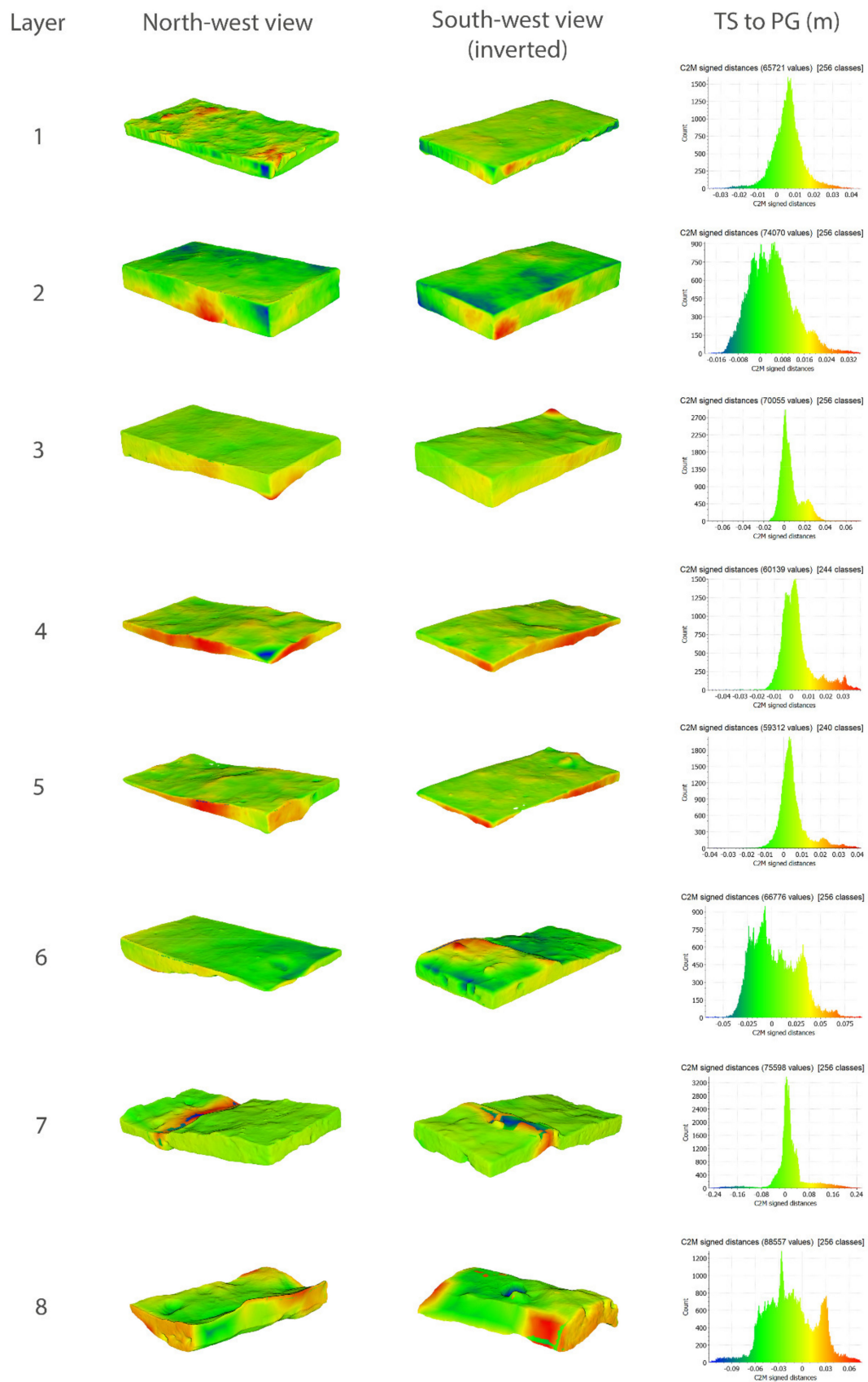


Figure 7. Comparison of the TS mesh onto the PG mesh by layer.

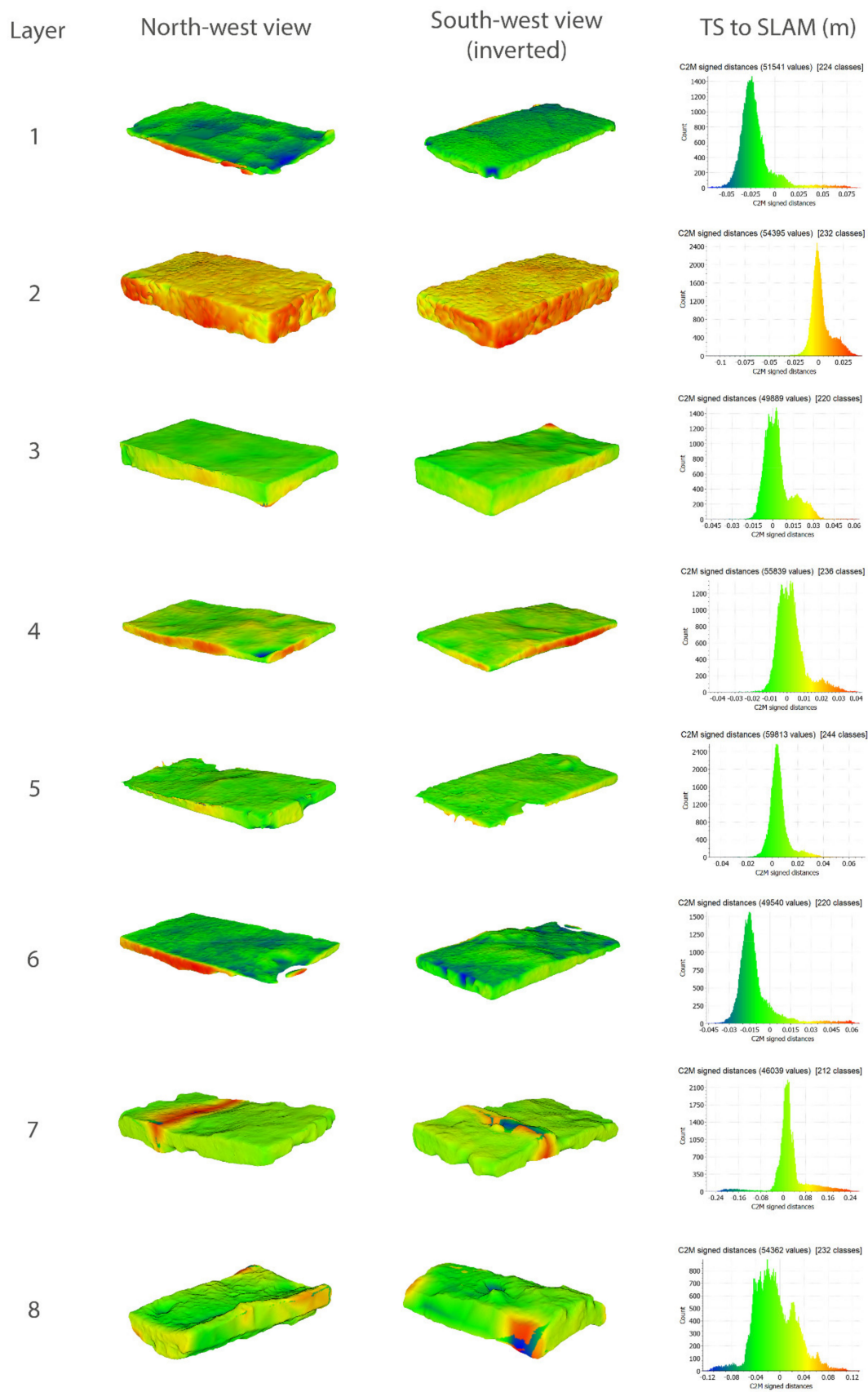


Figure 8. Comparison of the TS mesh onto the SLAM mesh by layer.

**Table 3.** Wilcoxon signed-ranks tests for differences in mesh and convex hull surface areas. Bold values are significant at  $\alpha = 0.05$ .

Comparison	Shapiro–Wilk $p$ -Value	Test Statistic	$p$
Mesh			
PG vs. TS	0.078	$t = 1.892, df = 7$	0.100
PG vs. SLAM	0.902	$t = 2.015, df = 7$	0.084
TS vs. SLAM	<b>0.025</b>	$V = 13$	0.547
Mesh vs. convex hull			
PG	0.215	$t = -9.547, df = 7$	<b>&lt;0.001</b>
TS	<b>&lt;0.001</b>	$V = 0$	<b>0.008</b>
SLAM	0.423	$t = -6.705, df = 7$	<b>&lt;0.001</b>
Convex hull			
PG vs. TS	0.058	$t = 3.190, df = 7$	<b>0.006</b>
PG vs. SLAM	0.997	$t = -3.188, df = 7$	<b>0.015</b>
TS vs. SLAM	0.105	$t = -5.383, df = 7$	<b>0.001</b>

To evaluate the surface estimates of the three models simultaneously within each modelling technique repeated measures ANOVA were run. The first set compared differences in volume or surface areas estimated from SLAM, PG and TS methods modeled using triangulated mesh. The second, assessed differences from these methods model using convex hulls. The results of these repeated measures ANOVA indicated that the residuals were not normally distributed, consequently we used Friedman test. The Friedman test of rank-order differences in surface area estimates per deposit for the three methods modeled using triangulated mesh shows that differences among methods across deposits are not consistent enough to be judged statistically significant (Friedman test statistic = 5.24, Kendall coefficient of concordance = 0.328,  $p = 0.072$ ). The same Friedman test comparison of surface areas modeled using convex hulls does indicate a statistically significant consistency in pattern of differences across the three methods (Friedman test statistic = 9.0, Kendall coefficient of concordance = 0.562,  $p = 0.011$ ). This result can be attributed to the over-representation of surface areas when hull models are made in relation to triangulated mesh models.

## 7.2. Volume Comparison

Table 4 reports estimates of volume in  $m^3$  by deposit with each method and modelling technique. Paired  $t$ -tests or Wilcoxon signed-ranks tests assessed pair-wise differences in estimated volumes within deposits for each method (SLAM, PG, or TS) across the two modelling techniques. The results in the first section of Table 5 indicate that there are no significant differences in the volumes of deposits between the meshed SLAM, PG, and TS models when each mesh model is compared with another mesh model. The results in the second section of Table 5 indicate that within each method, volumes estimated using convex hulls are consistently greater than those estimated using triangulated mesh. Convex hull calculations tend to over-represent the volume of the mesh as concavities are ignored (Figure 9). While the extent of the over-representation varies, in general SLAM convex hulls over-represent volume the most, followed by PG. The least discrepancy is amongst the TS volume reconstructions, likely because of the reduced resolution (number of points) used in the meshing process. The difference in volume between meshes and convex hulls is especially apparent in the calculation of layer 7 (Table 4). The results in the third section of Table 5 indicate that there are significant differences in the volumes of deposits between the convex hull SLAM, PG, and TS models when each convex hull model is compared with another convex hull model. The increased surface variation in the SLAM and PG meshes is a likely cause of this, as the TS has less variation as a product of the lower number of points used in the convex hull calculation.

**Table 4.** Volumes of each layer by method and modelling technique in m<sup>3</sup>.

Deposit	Triangulated Mesh			Convex Hull			
	SLAM	PG	TS	SLAM	PG	TS	Artefact
1	0.119	0.256	0.228	0.332	0.369	0.284	0.010
2	0.580	0.593	0.571	0.732	0.654	0.592	0.330
3	0.424	0.440	0.411	0.579	0.566	0.465	0.200
4	0.203	0.204	0.194	0.312	0.309	0.241	0.030
5	0.176	0.176	0.157	0.345	0.304	0.237	0.030
6	0.205	0.268	0.261	0.353	0.436	0.313	0.180
7	0.286	0.261	0.251	0.518	0.309	0.360	0.250
8	0.101	0.085	0.126	0.164	0.142	0.150	0.210

**Table 5.** Wilcoxon signed-rank tests for differences in mesh and convex hull volumes. Bold values are significant at  $\alpha = 0.05$ .

Comparison	Shapiro–Wilk <i>p</i> -Value	Test Statistic	<i>p</i>
Mesh			
PG vs. TS	<b>0.010</b>	V = 28	0.195
PG vs. SLAM	<b>0.040</b>	V = 26	0.313
TS vs. SLAM	0.108	t = 0.778, df = 7	0.462
Mesh vs. convex hull			
PG	0.471	t = −6.751, df = 7	<b>&lt;0.001</b>
TS	0.436	t = −5.400, df = 7	<b>0.001</b>
SLAM	0.827	t = −8.180, df = 7	<b>&lt;0.001</b>
Convex hull			
PG vs. TS	0.244	t = 2.727, df = 7	<b>0.029</b>
PG vs. SLAM	0.417	t = −1.006, df = 7	0.348
TS vs. SLAM	0.784	t = −4.806, df = 7	<b>0.002</b>

The Friedman test of differences in volume estimates per deposit confirm these results. The result for the three methods modeled using triangulated mesh indicates that estimates are not statistically distinct (Friedman test statistic = 5.25, Kendall coefficient of concordance = 0.328,  $p = 0.072$ ). However, a visual inspection of the rank order of deposit volumes of each method shows indicative patterning (Figure 10). The TS estimates of deposit volumes are generally lower than the SLAM estimates, which are generally lower than the PG estimates. The SLAM and PG point clouds have higher resolution point clouds than the TS point clouds and, therefore, record more surface variability. This can result in an increase in volume, as small variations are recorded that the TS does not record. As noted, this variability, however, is not statistically distinct. However, Friedman test results using convex hulls show a consistent pattern of differences in volume estimates of the three methods (Friedman test statistic = 9.0, Kendall coefficient of concordance = 0.562,  $p = 0.011$ ), again the result of overrepresentation of volume in convex hull models.

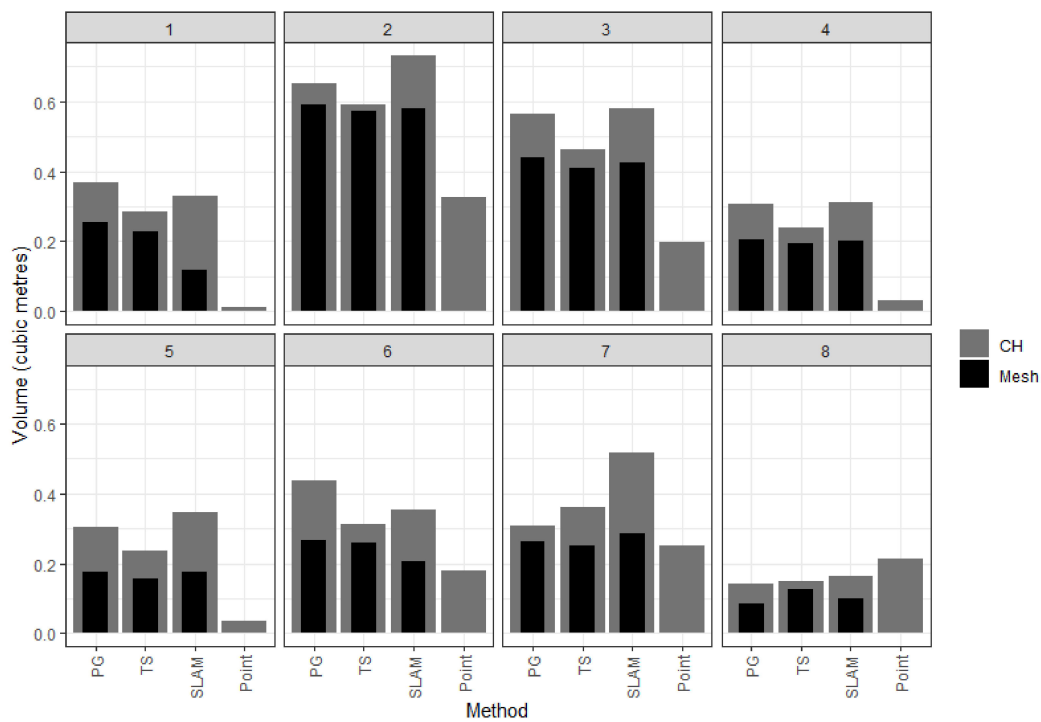


Figure 9. Comparison of the mesh and convex hull volumes. Point = volumes generated from artefact points.

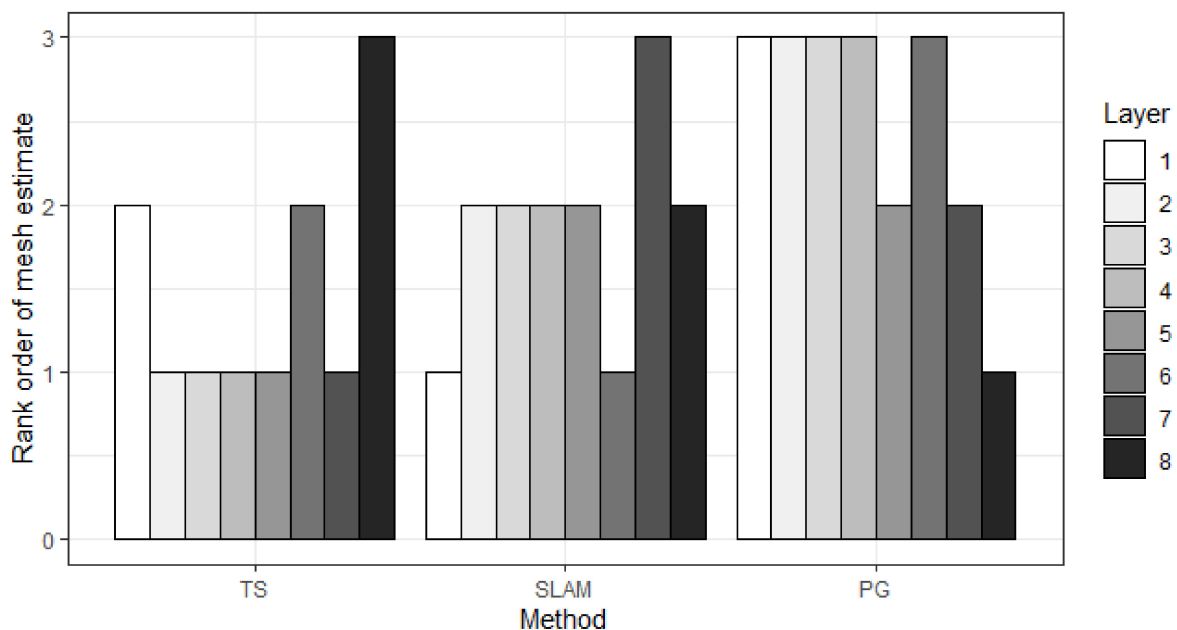
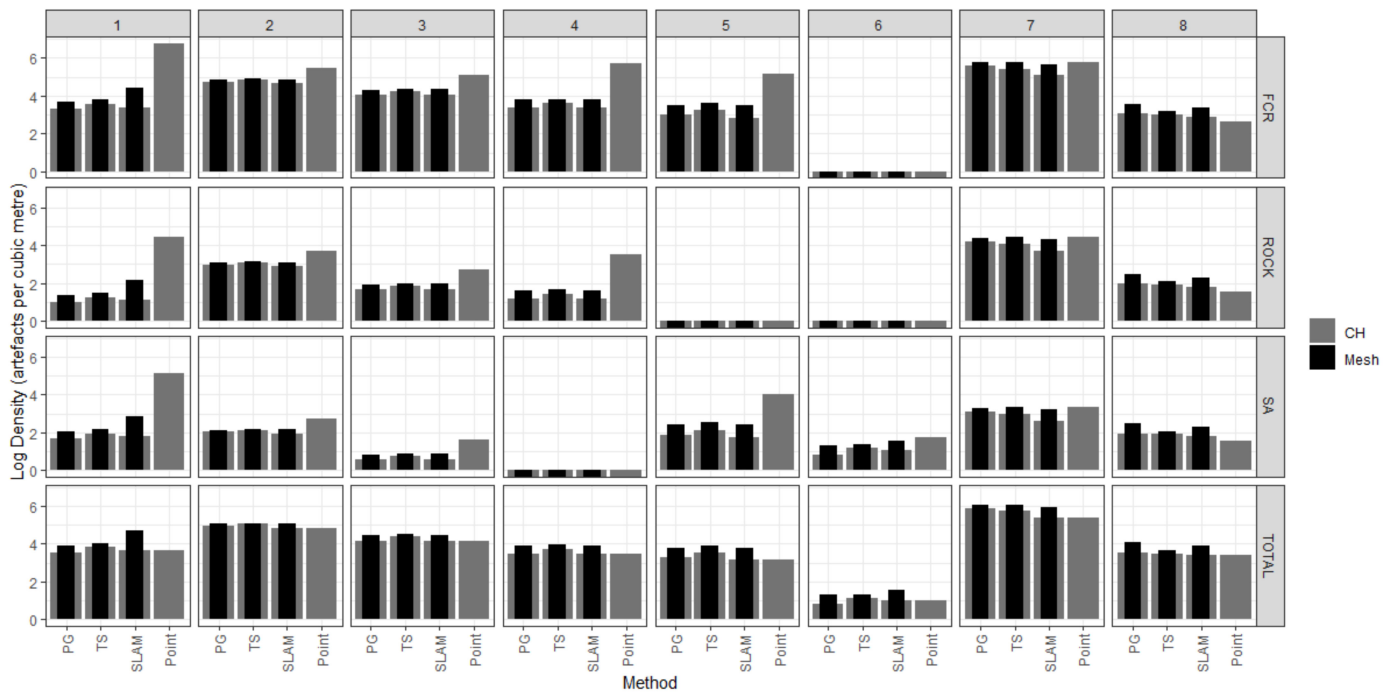


Figure 10. Rank orders of volumes for each deposit across methods modelled using triangulated mesh.

### 7.3. Artefact Densities

The deposits of EA231 contained vastly different amounts of artifactual material (Figure 11, Table 6). Without considering the volume of deposits, it would be easy to conclude that layers 2 and 7 of EA231 contained large, almost equal, amounts of material, with layer 4 containing much less material. This would be an obvious misunderstanding of the spatial patterning of artifactual material, as it is necessary to calculate the volume of deposits to establish artefact densities to identify spatial patterning within EA231. These

artefact densities were calculated using the deposit volume estimates of the meshes and convex hulls of the three different acquisition methods. This simplistic analysis of the 3D data in relation to artefact distributions demonstrates that layer 7 has more than double the artefact density of layer 2, and layer 4 with much lower artefact frequencies than layer 2 has densities of almost a third of that deposit.



**Figure 11.** Visual comparison of the artefact densities ( $m^3$ ) for each artefact type and layer, by method. Note  $y$ -axis is log-transformed.

**Table 6.** Density of artefacts by layer for each object type in  $m^3$ . FCR = fire-cracked rock; rock = natural rock; SA = stone artefact. Mesh = triangulated mesh.

Layer	n.	PG		TS		SLAM		Artefact Point
		Mesh	CH	Mesh	CH	Mesh	CH	CH
<i>FCR</i>								
1	10	39.13	27.14	43.9	35.26	84.35	30.11	867.75
2	76	128.14	116.16	132.99	128.34	131.01	103.87	232.15
3	33	75.03	58.26	80.35	71.02	77.88	57.02	167.09
4	9	44.11	29.16	46.35	37.4	44.38	28.85	304.53
5	6	34.02	19.76	38.33	25.28	34.03	17.38	171.58
6	0	0	0	0	0	0	0	0
7	83	317.66	268.63	330.78	230.28	290.66	160.19	331.9
8	3	35.09	21.19	23.72	19.99	29.85	18.27	14.01
<i>Rock</i>								
1	1	3.91	2.71	4.39	3.53	8.43	3.01	86.78
2	13	21.92	19.87	22.75	21.95	22.41	17.77	39.71
3	3	6.82	5.3	7.3	6.46	7.08	5.18	15.19
4	1	4.9	3.24	5.15	4.16	4.93	3.21	33.84
5	0	0	0	0	0	0	0	0
6	0	0	0	0	0	0	0	0
7	21	80.37	67.97	83.69	58.26	73.54	40.53	83.97
8	1	11.7	7.06	7.91	6.66	9.95	6.09	4.67

Table 6. Cont.

Layer	n.	PG		TS		SLAM		Artefact Point
		Mesh	CH	Mesh	CH	Mesh	CH	CH
<i>Stone Artefact</i>								
1	2	7.83	5.43	8.78	7.05	16.87	6.02	173.55
2	5	8.43	7.64	8.75	8.44	8.62	6.83	15.27
3	1	2.27	1.77	2.43	2.15	2.36	1.73	5.06
4	0	0	0	0	0	0	0	0
5	2	11.34	6.59	12.78	8.43	11.34	5.79	57.19
6	1	3.73	2.3	3.84	3.2	4.87	2.84	5.62
7	7	26.79	22.66	27.9	19.42	24.51	13.51	27.99
8	1	11.7	7.06	7.91	6.66	9.95	6.09	4.67
<i>Total</i>								
1	13	50.87	35.28	57.07	45.83	109.65	39.14	39.14
2	94	158.49	143.67	164.48	158.74	162.03	128.48	128.48
3	37	84.12	65.33	90.09	79.63	87.32	63.93	63.93
4	10	49.01	32.4	51.5	41.56	49.31	32.06	32.06
5	8	45.36	26.35	51.11	33.7	45.37	23.17	23.17
6	1	3.73	2.3	3.84	3.2	4.87	2.84	2.84
7	111	424.82	359.25	442.37	307.97	388.72	214.23	214.23
8	5	58.49	35.32	39.53	33.31	49.75	30.45	30.45

The more useful aspect of our analysis is not the simplistic calculation of densities from EA231, rather the quantification of differences of artefact densities produced by the volume estimates of the three different acquisition methods. As shown by the statistical tests discussed above, the mesh volume estimates of the three methods do not differ significantly. The variation in artefact densities in those deposits reflects this. The artefact densities associated with the convex hull estimates of volume show more variability, as those models accentuate the volume differences of a deposit. The artefact densities calculated using the volume estimates of the artefact point convex hulls further distort patterning, as they greatly under-represent the artefact densities because those models greatly over-represent the volumes of deposits.

## 8. Discussion

One reason for recording deposits during excavation is to enable stratigraphic analysis. In practice, recording deposits is complex, as where a deposit begins and ends can be difficult to determine. In some cases, a change in deposit is only noticed retrospectively either when the next deposit is being excavated or at the end of the excavation when profiles are drawn. The profile of EA231 (Figure 2) demonstrates some of the issues, as some deposits in this profile (which are shown unnumbered in that profile) were only identified during final recording and were not recorded with TS, PG, or SLAM during excavation. This is unavoidable, as it is difficult, if not impossible, to identify all deposits during the excavation process. This does, however, call into question the utility of creating 3D representations of excavated deposits. Deposits represent the process of excavation, the decisions that were made, and the places where excavators identified differences in the matrix significant enough to meet their criterion for defining a new deposit. Analytically and for archaeological investigation, this means that the volumes of deposits recorded during excavation must be carefully considered with other archaeological data such as stratigraphic drawings, artefact densities, and data from related excavations, before their bounds and densities are accepted. These ambiguities surrounding deposits are issues that must be dealt with regardless of which data acquisition method (e.g., TS, PG, and SLAM) is used. However, as the resolution at which TS is recorded is lower than PG and SLAM, using TS does make some decisions easier and provide the ability to “reconstruct” or revise the extents of previously excavated deposits.

The various methods used to calculate volumes of deposits affect the definition and essential qualities of deposits. The mesh is a triangulation of the points that represent the exterior of the volume, whereas the convex hull represents the smallest convex surface area around a set of points. A convex hull will only mimic a triangulated mesh when there is little concave variation in the surface of the mesh. This is obviously ill-suited for most archaeological data, as surface variation can occur as both convex and concave shapes. Layer 7 exemplifies this as a concave shape that is represented by its base means that a larger area is represented by the volume than actually exists (Figure 5). As the statistical tests above showed, while they may not be as pronounced as in layer 7, the convex hull models over-represent the volumes of the deposits compared to the triangulated meshes.

Our statistical analysis indicates that there are no significant differences between the triangulated mesh surface areas and volumes of deposits created from the TS, PG, and SLAM data. There does appear to be some patterning in the data that suggests that TS mesh volume estimates of deposits are smaller than SLAM meshes of those deposits, with PG volumes being largest, but that patterning is neither consistent nor statistically significant. Larger volumes will of course result in the calculation of lower artifact densities, while smaller volumes result in higher densities.

The statistical result that there are no significant differences between the surface area or volume estimates produced by TS, PG, and SLAM triangular meshes and data acquisition methods suggests that other factors should be considered when deciding which method to use.

### *8.1. Time*

The amount of time to implement the TS, PG, or SLAM method varies both for in-field recording and subsequent processing. While measurements were not taken on the exact time spent during the acquisition and processing of data for each recording method, some general observations can be made. Overall, the in-field recording of TS data is the quickest, with SLAM and PG taking about the same time. Each method can vary depending on the proficiency of the operator, the weather on the day, and the complexity of the subject. A deposit with a more complex shape, such as layers 7 or 8, will take more time than a relatively simple deposit such as layer 2. With SLAM, the initial setup of bases that were recorded with a total station were used over the course of the excavation, and so it was only the actual scanning that needed to occur, as was the case with PG and the attributed targets. What was required for both of those methods was also that the area be cleared of excavation equipment and people, more so than would occur during the standard photography of a unit. TS recording does require areas to be generally free of excavators, but it is not necessary to remove all excavation gear. That TS recording was more seamless in terms of workflow, as the total station is already part of the provenancing of artifacts and other materials during the excavation. However, TS recording a more complex shaped volume such as layer 8 will require more points to capture its shape and, therefore, take longer than the use of PG or SLAM.

The amount of time to process the data once they have been recorded also varies between the three methods. The SLAM data arguably took the longest active processing, that being where an operator's attention was required to align and clean the data before producing a point cloud of a deposit. PG took the most computer processing time but required less from the operator in that it could mostly be automated and processed in batches. Once the meshes were created, these then needed to be edited into volumes as outlined above, which required active researcher attention. TS data processing was mostly manually done by an operator, but the points used for each deposit were relatively few and took little time to isolate and triangulate into a volume.

### *8.2. Cost*

There are differences in the monetary costs of each method. While the price and availability of different technologies varies from region to region, general trends can be

noted. TS range in price but usually cost in the tens of thousands of dollars, and for efficient data capture on the scale required for surface reconstructions, a robotic TS is required, which are generally more expensive. A TS can, however, be used with minimal training and usually comes with the software required to process the raw data. PG requires a camera and ideally a tripod to capture the data and PG software, which can be open-source or proprietary. While cameras can vary dramatically in cost, a camera of sufficient quality is relatively inexpensive. PG is the most cost-effective method of these three and can be implemented and processed successfully with minimal training. By comparison, SLAM is more expensive, as the machinery costs tens of thousands of dollars, but also requires proprietary software to process the data. There is some open-source software such as CloudCompare, which can be used for data processing, but often obtaining data to these requires outputting data from the machine through a proprietary software. As with the other methods, SLAM can be learnt relatively quickly.

## 9. Conclusions

The application of 3D recording to archaeological excavations will continue to become commonplace in archaeological inquiry. This will result in the modification and revising of workflows to account for these methods, but the extent to which this needs to occur is important to consider. Based on the above, it was found that obtaining PG and SLAM data in addition to TS data for each deposit was largely redundant if deposit volumes were the goal. Volumes created from TS data create a statistically similar volume in less time, both in the field and during the processing of that data in the lab. PG volumes, however, provide what can be considered as the most “real” visualization.

These conclusions are based on the current state of technology, both in terms of the instruments required for TS, PG, and SLAM data acquisition and the processing of that data into 3D surface and volumetric entities. We suspect that with future developments, the advantages and disadvantages of the three methods will shift, and indeed, the methods will be replaced by new approaches. Currently, for recording purposes, a PG or SLAM model could be made of the end of an excavation, of which the TS volumes could then be enclosed within for visualization. This also allows for the representation of any deposits identified at the end of excavation that may have been missed. However, their surface variability within the trench will not be possible to reconstruct.

There may be a perceived benefit of recording every layer to a high degree of detail in that it creates a record of the excavation. However, the analytical benefit of this must be weighed against the time to complete it. It must also be carefully considered what is being recorded. The deposits represented, while broadly representative of the extents of the archaeological deposits they were recorded as, are equally if not more so representative of the decisions that went into excavation and recording.

**Supplementary Materials:** The following are available online at <https://www.mdpi.com/article/10.3390/rs13194015/s1>, File S1: R scripts and associated volumetric and density data used in the analysis.

**Author Contributions:** Conceptualization, J.E. and T.N.L.; methodology, J.E., P.P., S.M., T.M. and M.B.; software, J.E., P.P. and M.B.; validation, J.E., M.B., B.F. and T.N.L.; formal analysis, J.E., M.B., B.F. and T.N.L.; investigation, J.E., M.B., B.F. and T.N.L.; resources, J.E., P.P., S.M. and T.N.L.; data curation, J.E.; writing—original draft preparation, J.E. and T.N.L.; writing—review and editing, J.E., P.P., M.B., S.M., T.M., B.F. and T.N.L.; visualization, J.E. and M.B.; supervision, J.E. and T.N.L.; project administration, J.E. and T.N.L.; funding acquisition, T.N.L. All authors have read and agreed to the published version of the manuscript.

**Funding:** Te Pūnaha Matatini, Michael Fay, and the Faculty of Arts, University of Auckland.

**Institutional Review Board Statement:** Not applicable.

**Informed Consent Statement:** Not applicable.

**Data Availability Statement:** R scripts and associated data are available as Supplementary Files.

**Acknowledgments:** We gratefully acknowledge and thank Ngāti Hei for their mana whenua cultural support and permission to undertake archaeological research on the island. The Fay and Richwhite families have been very generous in providing access to the island and support while there. We thank Simon Holdaway, Rebecca Phillipps, Alex Jorgensen, and Louise Furey for discussions and contributions to our research. Seline McNamee assisted with the creation of Figure 2.

**Conflicts of Interest:** The authors declare no conflict of interest.

## References

- Emmitt, J.J.; Mackrell, T.; Armstrong, J. Digital Modelling in Museum and Private Collections: A Case Study on Early Italic Armour. *J. Comput. Appl. Archaeol.* **2021**, *4*, 63–78. [\[CrossRef\]](#)
- Berggren, Å.; Dell’Unto, N.; Forte, M.; Haddow, S.; Hodder, I.; Issavi, J.; Lercari, N.; Mazzucato, C.; Mickel, A.; Taylor, J.S. Revisiting reflexive archaeology at Çatalhöyük: Integrating digital and 3D technologies at the trowel’s edge. *Antiquity* **2015**, *89*, 433–448. [\[CrossRef\]](#)
- Porter, S.T.; Huber, N.; Hoyer, C.; Floss, H. Portable and low-cost solutions to the imaging of Paleolithic art objects: A comparison of photogrammetry and reflectance transformation imaging. *J. Archaeol. Sci. Rep.* **2016**, *10*, 859–863. [\[CrossRef\]](#)
- Porter, S.T.; Roussel, M.; Soressi, M. A Simple Photogrammetry Rig for the Reliable Creation of 3D Artifact Models in the Field. *Adv. Archaeol. Pract. J. Soc. Am. Archaeol.* **2016**, *4*, 71–86. [\[CrossRef\]](#)
- Secci, M.; Demesticha, S.; Jimenez, C.; Papadopoulou, C.; Katsouri, I. A Living Shipwreck: An integrated three-dimensional analysis for the understanding of site formation processes in archaeological shipwreck sites. *J. Archaeol. Sci. Rep.* **2021**, *35*, 102731. [\[CrossRef\]](#)
- Emmitt, J.; Littleton, J.; Young, R.; Phillipps, R. Digitizing Roonka: The creation of a 3D representation from archival records. *Digit. Appl. Archaeol. Cult. Herit.* **2019**, *13*, e00094. [\[CrossRef\]](#)
- Gavryushkina, M. The potential and problems of volumetric 3D modeling in archaeological stratigraphic analysis: A case study from Chlorakas-Palloures, Cyprus. *Digit. Appl. Archaeol. Cult. Herit.* **2021**, *21*, e00184. [\[CrossRef\]](#)
- Dibble, H.L. Measurement of Artifact Provenience with an Electronic Theodolite. *J. Field Archaeol.* **1987**, *14*, 229.
- Dibble, H.L.; McPherron, S.P. On the Computerization of Archaeological Projects. *J. Field Archaeol.* **1988**, *15*, 431–440. [\[CrossRef\]](#)
- Holdaway, S.; Irwin, G. Electronic recording systems used during the excavation of S11/20, Ponui Island, Hauraki Gulf. *Archaeol. N. Z.* **1993**, *36*, 27–37.
- Losier, L.M.; Pouliot, J.; Fortin, M. 3D geometrical modeling of excavation units at the archaeological site of Tell ‘Acharneh (Syria). *J. Archaeol. Sci.* **2007**, *34*, 272–288. [\[CrossRef\]](#)
- Phillipps, R.; Holdaway, S.J.; Ramsey, R.; Wendrich, W.; Emmitt, J. Approaches to Paleoenvironment and Landscape Use. In *The Desert Fayum Reinvestigated. The Early to Mid-Holocene Landscape Archaeology of the Fayum North Shore, Egypt*; Cotsen Institute of Archaeology Press: Los Angeles, CA, USA, 2017; p. 17.
- McPherron, S.J.P. Artifact orientations and site formation processes from total station proveniences. *J. Archaeol. Sci.* **2005**, *32*, 1003–1014. [\[CrossRef\]](#)
- Casana, J.; Laugier, E.J.; Hill, A.C.; Reese, K.M.; Ferwerda, C.; McCoy, M.D.; Ladefoged, T. Exploring archaeological landscapes using drone-acquired lidar: Case studies from Hawai’i, Colorado, and New Hampshire, USA. *J. Archaeol. Sci. Rep.* **2021**, *39*, 103133. [\[CrossRef\]](#)
- McCoy, M.D.; Casana, J.; Hill, A.C.; Laugier, E.J.; Mulrooney, M.A.; Ladefoged, T.N. Unpiloted Aerial Vehicle Acquired Lidar for Mapping Monumental Architecture. *Adv. Archaeol. Pract. J. Soc. Am. Archaeol.* **2021**, *9*, 160–174. [\[CrossRef\]](#)
- Opitz, R.S.; Ryzewski, K.; Cherry, J.F.; Moloney, B. Using airborne LiDAR Survey to explore historic-era archaeological landscapes of Montserrat in the eastern Caribbean. *J. Field Archaeol.* **2015**, *40*, 523–541. [\[CrossRef\]](#)
- Masini, N.; Coluzzi, R.; Lasaporana, R. On the Airborne Lidar Contribution in Archaeology: From Site Identification to Landscape Investigation. In *Laser Scanning, Theory and Applications*; Wang, C.C., Ed.; IntechOpen: London, UK, 2011; pp. 263–290. [\[CrossRef\]](#)
- McIvor, I.H. Monumental Ideology: A GIS Spatial Analysis of Interior Features of Matakawau Pā, Ahuahu (Stingray Point Pā, Great Mercury Island), New Zealand. *J. Polyn. Soc.* **2015**, *124*, 269–302. [\[CrossRef\]](#)
- Larsen, B.P.; Holdaway, S.J.; Fanning, P.C.; Mackrell, T.; Shiner, J.I. Shape as an outcome of formation history: Terrestrial Laser Scanning of shell mounds from far north Queensland, Australia. *Quat. Int.* **2017**, *427*, 5–12. [\[CrossRef\]](#)
- Emmitt, J.; Allely, K.; Davies, B.; Hoffman, E.; Holdaway, S.J. Preliminary archaeological survey and remote-sensing of shell mounds at Kwokkunum, Albatross Bay, Cape York Peninsula, Australia. *Qld. Archaeol. Res.* **2020**, *23*, 9–24. [\[CrossRef\]](#)
- Rabbia, A.; Sammartano, G.; Spanò, A. Fostering Etruscan heritage with effective integration of UAV, TLS and SLAM-based methods. In Proceedings of the IMEKO TC-4 International Conference on Metrology for Archaeology and Cultural Heritage, Trento, Italy, 22–24 October 2020; pp. 322–327.
- Clark, C.M.; Olstad, C.S.; Buhagiar, K.; Gambin, T. Archaeology via underwater robots: Mapping and localization within maltese cistern systems. In Proceedings of the 10th International Conference on Control, Automation, Robotics and Vision, Hanoi, Vietnam, 17 December 2008; pp. 662–667.
- Magnani, M.; Douglass, M.; Schroder, W.; Reeves, J.; Braun, D.R. The Digital Revolution to Come: Photogrammetry in Archaeological Practice. *Am. Antiq.* **2020**, *85*, 737–760. [\[CrossRef\]](#)

24. Bolles, R.C.; Baker, H.H.; Marimont, D.H. Epipolar-plane image analysis: An approach to determining structure from motion. *Int. J. Comput. Vis.* **1987**, *1*, 7–55. [[CrossRef](#)]
25. Douglass, M.; Lin, S.; Chodoronek, M. The Application of 3D Photogrammetry for In-Field Documentation of Archaeological Features. *Adv. Archaeol. Pract. J. Soc. Am. Archaeol.* **2015**, *3*, 136–152. [[CrossRef](#)]
26. López, J.A.B.; Jiménez, G.A.; Romero, M.S.; García, E.A.; Martín, S.F.; Medina, A.L.; Guerrero, J.A.E. 3D modelling in archaeology: The application of Structure from Motion methods to the study of the megalithic necropolis of Panoria (Granada, Spain). *J. Archaeol. Sci. Rep.* **2016**, *10*, 495–506. [[CrossRef](#)]
27. McCarthy, J. Multi-image photogrammetry as a practical tool for cultural heritage survey and community engagement. *J. Archaeol. Sci.* **2014**, *43*, 175–185. [[CrossRef](#)]
28. De Reu, J.; Plets, G.; Verhoeven, G.; De Smedt, P.; Bats, M.; Cherretté, B.; De Maeyer, W.; Deconynck, J.; Herremans, D.; Laloo, P.; et al. Towards a three-dimensional cost-effective registration of the archaeological heritage. *J. Archaeol. Sci.* **2013**, *40*, 1108–1121. [[CrossRef](#)]
29. Gomez, C. Digital photogrammetry and GIS-based analysis of the bio-geomorphological evolution of Sakurajima Volcano, diachronic analysis from 1947 to 2006. *J. Volcanol. Geotherm. Res.* **2014**, *280*, 1–13. [[CrossRef](#)]
30. Dell’Unto, N.; Landeschi, G.; Apel, J.; Poggi, G. 4D recording at the trowel’s edge: Using three-dimensional simulation platforms to support field interpretation. *J. Archaeol. Sci. Rep.* **2017**, *12*, 632–645. [[CrossRef](#)]
31. Scott, C.B.; Roosevelt, C.H.; Nobles, G.R.; Luke, C. Born-Digital Logistics: Impacts of 3D Recording on Archaeological Workflow, Training, and Interpretation. *Open Archaeol.* **2021**, *7*, 574–588. [[CrossRef](#)]
32. Peng, F.; Lin, S.C.; Guo, J.; Wang, H.; Gao, X. The Application of SfM Photogrammetry Software for Extracting Artifact Provenience from Palaeolithic Excavation Surfaces. *J. Field Archaeol.* **2017**, *42*, 326–336. [[CrossRef](#)]
33. Sapirstein, P. A high-precision photogrammetric recording system for small artifacts. *J. Cult. Herit.* **2018**, *31*, 33–45. [[CrossRef](#)]
34. Bandini, F.; Sunding, T.P.; Linde, J.; Smith, O.; Jensen, I.K.; Köppl, C.J.; Butts, M.; Bauer-Gottwein, P. Unmanned Aerial System (UAS) observations of water surface elevation in a small stream: Comparison of radar altimetry, LIDAR and photogrammetry techniques. *Remote Sens. Environ.* **2020**, *237*, 111487. [[CrossRef](#)]
35. Wendrich, W.; Simpson, B.; Elgewely, E. Karanis in 3D: Recording, Monitoring, Recontextualizing, and the Representation of Knowledge and Conjecture. *Near East. Archaeol.* **2014**, *77*, 233–237. [[CrossRef](#)]
36. Lambers, K.; Eisenbeiss, H.; Sauerbier, M.; Kupferschmidt, D.; Gaisecker, T.; Sotoodeh, S.; Hanusch, T. Combining photogrammetry and laser scanning for the recording and modelling of the Late Intermediate Period site of Pinchango Alto, Palpa, Peru. *J. Archaeol. Sci.* **2007**, *34*, 1702–1712. [[CrossRef](#)]
37. Lerma, J.L.; Navarro, S.; Cabrelles, M.; Villaverde, V. Terrestrial laser scanning and close range photogrammetry for 3D archaeological documentation: The Upper Palaeolithic Cave of Parpalló as a case study. *J. Archaeol. Sci.* **2010**, *37*, 499–507. [[CrossRef](#)]
38. Verhoeven, G. Mesh Is More—Using All Geometric Dimensions for the Archaeological Analysis and Interpretative Mapping of 3D Surfaces. *J. Archaeol. Method Theory* **2017**, *24*, 999–1033. [[CrossRef](#)]
39. Holata, L.; Plzák, J.; Světlík, R.; Fonte, J. Integration of Low-Resolution ALS and Ground-Based SfM Photogrammetry Data. A Cost-Effective Approach Providing an ‘Enhanced 3D Model’ of the Hound Tor Archaeological Landscapes (Dartmoor, South-West England). *Remote Sens.* **2018**, *10*, 1357. [[CrossRef](#)]
40. Martínez-Fernández, A.; Benito-Calvo, A.; Campaña, I.; Ortega, A.I.; Karampaglidis, T.; de Castro, J.M.B.; Carbonell, E. 3D monitoring of Paleolithic archaeological excavations using terrestrial laser scanner systems (Sierra de Atapuerca, Railway Trench sites, Burgos, N Spain). *Digit. Appl. Archaeol. Cult. Herit.* **2020**, *19*, e00156. [[CrossRef](#)]
41. Orengo, H.A. Combining terrestrial stereophotogrammetry, DGPS and GIS-based 3D voxel modelling in the volumetric recording of archaeological features. *ISPRS J. Photogramm. Remote Sens.* **2013**, *76*, 49–55. [[CrossRef](#)]
42. Dell’Unto, N.; Landeschi, G.; Touati, A.-M.L.; Dellepiane, M.; Callieri, M.; Ferdani, D. Experiencing Ancient Buildings from a 3D GIS Perspective: A Case Drawn from the Swedish Pompeii Project. *J. Archaeol. Method Theory* **2016**, *23*, 73–94. [[CrossRef](#)]
43. Rodríguez-Gonzálvez, P.; Fernández-Palacios, B.J.; Muñoz-Nieto, Á.L.; Arias-Sanchez, P.; González-Aguilera, D. Mobile LiDAR System: New Possibilities for the Documentation and Dissemination of Large Cultural Heritage Sites. *Remote Sens.* **2017**, *9*, 189. [[CrossRef](#)]
44. Roosevelt, C.H.; Cobb, P.; Moss, E.; Olson, B.R.; Ünlüsoy, S. Excavation is Destruction Digitization: Advances in Archaeological Practice. *J. Field Archaeol.* **2015**, *40*, 325–346. [[CrossRef](#)]
45. Nobles, G.R.; Roosevelt, C.H. Filling the Void in Archaeological Excavations: 2D Point Clouds to 3D Volumes. *Open Archaeol.* **2021**, *7*, 589–614. [[CrossRef](#)]
46. Emmitt, J.; Sefton, B.; Phillipps, R.; Wendrich, W.; Holdaway, S. Reimag(in)ing the Past: Adding the Third Dimension to Archaeological Section Drawings. *Adv. Archaeol. Pract. J. Soc. Am. Archaeol.* **2017**, *5*, 44–53. [[CrossRef](#)]
47. Edson, S. Human Ecology and Prehistoric Settlement on Some Offshore Islands (East Cape to Cape Reinga). Ph.D. Thesis, University of Auckland, Auckland, New Zealand, 1973.
48. Furey, L. *Great Mercury Island: Archaeological Site Survey Forestry Development Block*; Report; PF Olsen Ltd.: Rotorua, New Zealand, 1983.
49. Furey, L.; Emmitt, J.; Wallace, R. Matakawau Stingray Point Pa excavation, Ahuahu Great Mercury Island 1955–56. *Rec. Auckl. Mus.* **2017**, *52*, 39–57. [[CrossRef](#)]

50. Golson, J. New Zealand Archaeological Association. *J. Polyn. Soc.* **1955**, *64*, 349–352.
51. Irwin, G. Archaeological excavations at Waipirau Pa, Ahuahu/Great Mercury Island, 1984. *Archaeol. N. Z.* **2015**, *58*, 200–212.
52. Davis, K.; Ladefoged, T.N. Variable horticulture within a small garden on Ahuahu (Great Mercury Island). *Rapa Nui J.* **2013**, *27*, 63–69.
53. Furey, L. Brief interim report for excavations on Ahuahu Great Mercury Island, June 2014 to February 2017. *Archaeol. N. Z.* **2017**, *60*, 45–67.
54. Furey, L.; Phillipps, R.; Jorgensen, A.; Holdaway, S.J.; Ladefoged, T. Investigations on Ahuahu Great Mercury Island 2012. *Archaeol. N. Z.* **2013**, *56*, 156–163.
55. Holdaway, S.J.; Emmitt, J.; Furey, L.; Jorgensen, A.; O'Regan, G.; Phillipps, R.; Prebble, M.; Wallace, R.; Ladefoged, T.N. Māori settlement of New Zealand: The Anthropocene as a process. *Archaeol. Ocean.* **2019**, *54*, 17–34. [[CrossRef](#)]
56. Furey, L.; Phillipps, R.; Emmitt, J.; McAlister, A.; Holdaway, S. A large trolling lure shank from Ahuahu Great Mercury Island, New Zealand. *J. Polyn. Soc.* **2020**, *129*, 85–112. [[CrossRef](#)]
57. Prebble, M.; Anderson, A.J.; Augustinus, P.; Emmitt, J.; Fallon, S.J.; Furey, L.L.; Holdaway, S.J.; Jorgensen, A.; Ladefoged, T.N.; Matthews, P.J.; et al. Early tropical crop production in marginal subtropical and temperate Polynesia. *Proc. Natl. Acad. Sci. USA* **2019**, *116*, 8824–8833. [[CrossRef](#)]
58. McIvor, I.H.; Ladefoged, T.N. A multi-scalar analysis of Māori land use on Ahuahu (Great Mercury Island), New Zealand. *Archaeol. Ocean.* **2016**, *51*, 45–61. [[CrossRef](#)]
59. Wallace, R.; Holdaway, S.P.D. Archaeological charcoal analysis in New Zealand. *J. Pac. Archaeol.* **2017**, *8*, 17–30.
60. Phillipps, R. Interim report on archaeological investigations Ahuahu Great Mercury Island, November 2012–February 2014. *Archaeol. N. Z.* **2014**, *57*, 215–228.
61. Holdaway, S.; Emmitt, J.; Phillipps, R.; Masoud-Ansari, S. A Minimalist Approach to Archaeological Data Management Design. *J. Archaeol. Method Theory* **2019**, *26*, 873–893. [[CrossRef](#)]
62. Agisoft. *Agisoft Metashape Professional*; Version 1.7.2; Agisoft: St. Petersburg, Russia, 2021.
63. Landeschi, G.; Apel, J.; Lundström, V.; Storå, J.; Lindgren, S.; Dell'Unto, N. Re-enacting the sequence: Combined digital methods to study a prehistoric cave. *Archaeol. Anthropol. Sci.* **2019**, *11*, 2805–2819. [[CrossRef](#)]
64. Katsianis, M.; Tshipidis, S.; Kotsakis, K.; Kousoulakou, A. A 3D digital workflow for archaeological intra-site research using GIS. *J. Archaeol. Sci.* **2008**, *35*, 655–667. [[CrossRef](#)]
65. Cignoni, P.; Callieri, M.; Corsini, M.; Dellepiane, M.; Ganovelli, F.; Ranzuglia, G. *Meshlab: An Open-Source Mesh Processing Tool*; The Eurographics Association: Geneva, Switzerland, 2008. [[CrossRef](#)]